Quantifying the impact of the surface roughness of ice crystals on the backscattering properties for lidar-based remote sensing applications

Masanori Saito[1,*] and Ping Yang[1]

[1]Department of Atmospheric Sciences, Texas A&M University, College Station, TX, USA.

Corresponding author: Masanori Saito (masa.saito@tamu.edu)

Key Points:

- Sensitivities of the backscattering properties to the surface roughness of atmospheric ice crystals are theoretically investigated.
- The depolarization ratio is markedly sensitive to the degree of surface roughness of ice crystals.
- The lidar and depolarization ratios observed by CALIOP are well explained with the ice model with degree of surface roughness 0.03–0.15.

Abstract

Impacts of small-scale surface irregularities, or surface roughness, of atmospheric ice crystals on lidar backscattering properties are quantified. Geometric ice crystal models with various degrees of surface roughness and state-of-the-science light-scattering computational capabilities are used to simulate single-scattering properties across the entire practical size parameter range. The simulated bulk lidar and depolarization ratios of polydisperse ice crystals at 532 nm are strongly sensitive to the degree of surface roughness. Comparisons of these quantities between the theoretical simulations and counterparts inferred from spaceborne lidar observations for cold cirrus clouds suggest a typical surface roughness range of 0.03–0.15, which is most consistent with direct measurements of scanning electron microscopic images. The degree of surface roughness needs to be accounted for to properly interpret lidar backscattering observations of ice clouds.

Plain Language Summary

Lidar (Light Detection and Ranging) instruments on satellites use reflected, or backscattered, laser beams to investigate ice clouds in the atmosphere. However, it has long been a challenge to interpret lidar signals, called backscattering properties, to accurately infer ice cloud characteristics. This study uses theoretical simulations to investigate how small-scale surface irregularities of ice crystals affect the lidar signals reflected from ice clouds. These simulations demonstrate the significant impacts of the small-scale surface irregularities of ice crystals on backscattering. Comparisons between the theoretical simulations and satellite lidar observations confirm the necessity to assume a moderate degree of small-scale surface irregularities to explain lidar observations of typical ice clouds.

1 Introduction

Atmospheric ice crystals often exhibit small-scale surface irregularities or roughness (Cross, 1968; Magee et al., 2014), which are caused mainly by depositional growth and sublimation under super- and sub-saturated conditions. Roughening of ice crystal surfaces has been observed via laboratory experiments (Pfalzgraff et al., 2010; Schnaiter et al., 2016; Butterfield et al., 2017) and in-situ measurements in cirrus clouds (Ulanowski et al., 2014; Magee et al., 2021). Compared to pristine ice crystals with smooth surfaces, those with roughened surfaces tend to have featureless phase function near backscattering angles, which corresponds to smaller asymmetry factor values. It has been demonstrated that surface roughness is a critical factor affecting passive remote sensing of ice cloud properties (Yang et al., 2008; van Diedenhoven et al., 2013; Hioki et al., 2016) and estimation of ice cloud radiative effects (Yi et al., 2013; Järvinen et al., 2018).

Surface roughness effects on the shortwave scattering properties of ice crystals have been theoretically investigated based mainly on the principles of geometric optics (Macke et al., 1996; Yang & Liou, 1998), because rigorous light-scattering computational methods lead to an enormous computational burden for typical ice crystal sizes in the ultra-violet to near-infrared spectral regime. However, geometric optics methods compute inaccurate single-scattering properties of ice crystals near the backscattering angle due to inherent limitations, particularly a lack of consideration of coherent backscattering enhancement (CBE). The more sophisticated Physical Geometric Optics Method (PGOM), implemented by either the surface-integral or volume-integral approach, fully considers phase interference of outgoing waves (Yang & Liou, 1996, 1997), and produces consistent numerical results (Yang et al., 2019). PGOM has been numerically implemented for relatively simple ice particles (e.g., columns and plates) and

aggregates of convex particles (e.g., 8-column aggregates; see Yang et al., 2019 and references cited therein).

The challenge in light-scattering computations for nonspherical particles, particularly in the case of large size parameters, has long hampered the accuracy of inferred ice cloud properties from lidar observations. Specifically, the physical interpretation of the backscattering properties of ice crystals, such as the lidar and depolarization ratios, is largely empirical (Zhou & Yang, 2015; Ding et al., 2016), leading to substantial uncertainties in inferred ice cloud quantities. As surface roughening in ice crystals is prevalent globally in ice clouds (van Diedenhoven et al., 2020), this study aims to quantify the impact of surface roughness based on a combination of state-of-the-science rigorous and approximate light-scattering computational algorithms applied to geometrically roughened ice crystal models.

2 Methods

2.1 Geometrically roughened ice crystal models

In this study, the degree of surface roughness is defined in terms of the variance (σ^2) of the two-dimensional Gaussian distribution $P(Z_x, Z_y)$ of local planar surface slopes (Liu et al., 2013; Saito & Yang, 2022a), which originates from a rough ocean surface model (Cox & Munk, 1954) and is described as

$$P(Z_x, Z_y) = \frac{1}{\pi\sigma^2} e^{-[(Z_x^2+Z_y^2)/\sigma^2]}, \quad (1)$$

where $Z_x = \partial Z/\partial x$ and $Z_y = \partial Z/\partial y$ are the slopes of local planar facets along two axes orthogonal to the normal direction Z in reference to an un-tilted regular crystal facet described

below. The original facets of a regular hexagonal column are discretized into many small triangular facets with a maximum facet length of approximately 1/40 of those original facets. These small facets are tilted according to the probability density of the surface slope defined by a 2D Gaussian distribution with the specified σ^2. Technical details on geometrically roughened ice crystal models are discussed in Liu et al. (2013). In this study, the macroscopic crystal shape is a regular hexagonal column with an aspect ratio of unity. Note that Okamoto et al. (2020) have investigated the backscattering properties of many other particle shapes without surface roughness.

Figure 1 illustrates geometrically roughened hexagonal column models with various degrees of surface roughness ranging from $\sigma^2 = 0$ (smooth) to 0.5 (severely roughened). A crystal surface with a higher degree of surface roughness has more complex texture. Neshyba et al. (2013) developed a stereographic method to estimate the surface roughness using scanning electron microscopic (SEM) images of an ice crystal, and found that surface roughness is well represented by a Weibull distribution with a shape parameter 0.7–0.95 (Butterfield et al., 2017). The Weibull distribution with a shape parameter of unity is equivalent to the 2D Gaussian distribution.

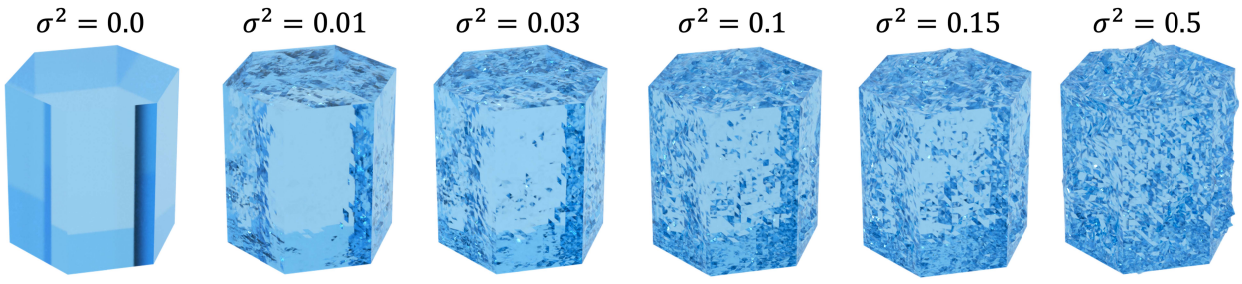

Figure 1. Illustration of geometric hexagonal column ice crystal models with degree of surface roughness 0, 0.01, 0.03, 0.1, 0.15, and 0.5.

100

101 2.2 Computational methods

102 To simulate the single-scattering properties of roughened ice crystals, we use the
103 numerically accurate Invariant-Imbedding T-matrix Method (IITM; Johnson, 1988; Bi & Yang,
104 2014; and references cited therein), for the largest possible size parameter cases. As the
105 computational burden increases exponentially with the size parameter, previous studies limited
106 simulations of geometrically roughened ice crystals to size parameter kD up to ~150, where the
107 modified wavenumber is $k = 2\pi/\lambda$, D is the particle maximum dimension, and λ is the
108 wavelength. Leveraging the computational capabilities provided by the Texas A&M University
109 High-Performance Research Computing (TAMU HPRC) facilities, we perform scattering
110 property simulations with IITM for roughened ice crystals with kD up to approximately 316.

111 For larger size parameters, we use the Improved Geometric Optics Method (IGOM; Yang
112 & Liou, 1996) which is a simplified form of PGOM. However, IGOM considers the ray
113 spreading effect but the ray-tracing procedure neglects the phase interference among scattered
114 waves associated fundamentally with different outgoing rays. This simplification results in
115 inaccuracy in backscattering directions. Saito and Yang (2022b) derived a semi-physical CBE
116 correction formula from Maxwell's equations to substantially reduce the systematic biases in the
117 backscattering properties computed with IGOM. With a combination of IITM for small-to-
118 moderate size parameters ($kD \leq 316$) and IGOM with a CBE correction (hereinafter referred to
119 as IGOM+CBE) for large size parameters, the single-scattering property simulations for
120 roughened ice crystals across the entire practical size parameter range are performed. For smooth
121 particles, IITM with an efficient scheme utilizing axial symmetry is performed for $kD \leq 464$,
122 and PGOM is performed for larger size parameters.

123

124 3 Results and Discussion

125 3.1 Phase matrix of roughened ice crystals

126 Figure 2 shows the six nonzero phase matrix elements of compact hexagonal ice crystals
127 with various degrees of surface roughness at wavelength 532 nm, which are computed with
128 IITM. Size parameter $kD = 316$ in these simulations corresponds to an ice crystal maximum
129 diameter of 26.8 μm. Halo peaks appear at scattering angles of approximately 22° and 46° in the
130 phase functions of smooth to moderately roughened ice crystals ($\sigma^2 < 0.1$) but are suppressed
131 for more roughened ice crystals (Bi & Yang, 2014). The angular variations of the phase matrix at
132 larger scattering angles seem sensitive to smaller degrees of surface roughness. For example, the
133 phase matrices at scattering angles around halo peaks are similar between smooth and slightly
134 roughened ($\sigma^2 = 0.01$) cases, while they are different at backward scattering angles (e.g.,
135 $> 120°$). Moreover, in Fig. 2a, the phase functions near the backscattering angle show distinct
136 differences between smooth and all roughened ice crystals.

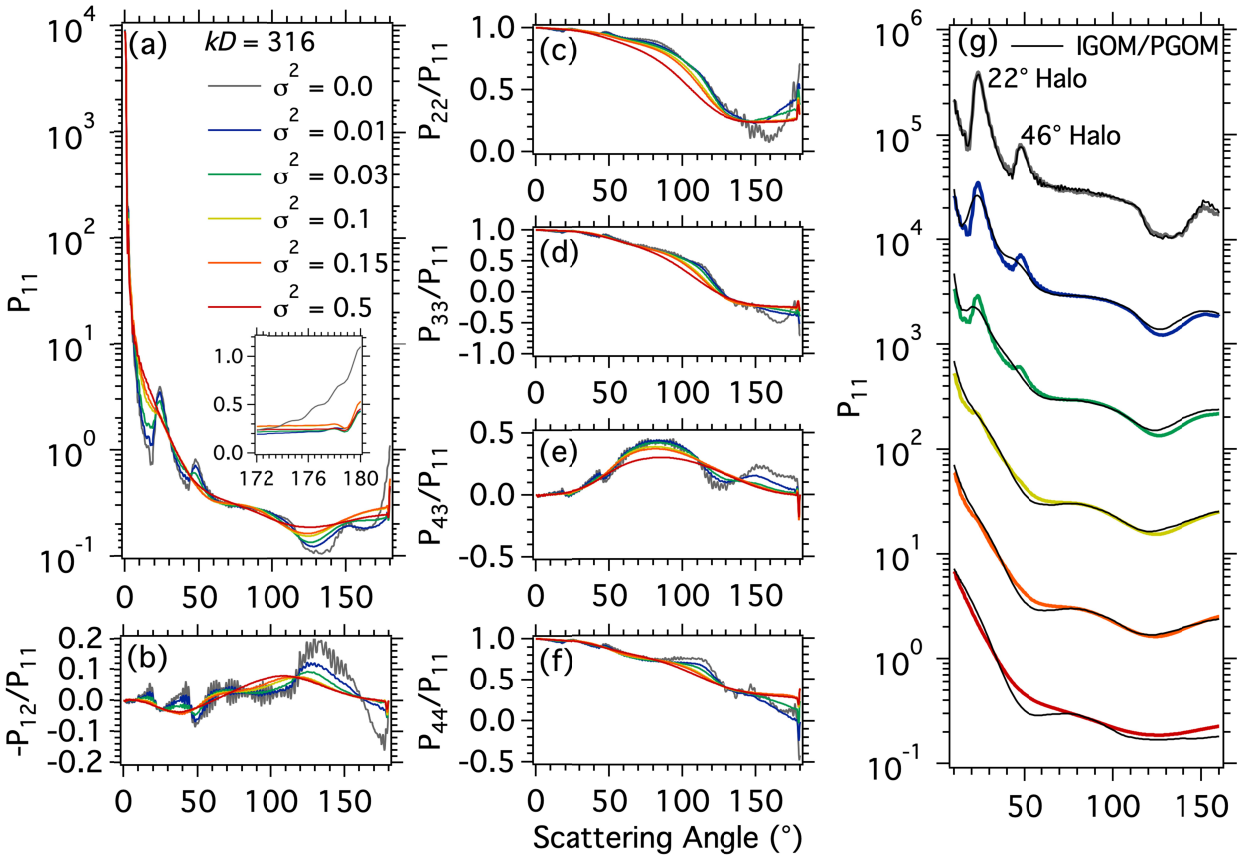

Figure 2. (a-f) Six independent phase matrix elements (labeled on y-axis) of ice crystals with various degrees of surface roughness denoted with different colors. (g) Phase function (P_{11}) curves computed with Invariant Imbedding T-matrix Method (bold lines with colors same as in panel (a)) and geometric optics methods (black lines) for the same six degrees of roughness, which are offset one order of magnitude apart.

In Fig. 2g, comparisons of the phase functions of smooth and roughened ice crystals are consistent between IITM and PGOM/IGOM across scattering angles for $\sigma^2 = 0.1$–0.5 and at backward scattering angles 90–160° for less roughened cases. Interestingly, the halo peaks computed with IITM show similar angular widths but weaker magnitudes of their peaks as roughness increases. In comparison, the counterparts computed with IGOM tend to be broadened

and more rapidly suppressed when the degree of surface roughness increases, particularly for the 46° halo peak (van Diedenhoven, 2014).

van de Hulst (1957) states that a pencil of light with its basal width of the order $l\lambda$ can retain its ray characteristics over a distance of the order $l^2\lambda$ according to the Fresnel–Huygens principle, where l and λ are the geometric width of the ray and wavelength of light. Ding et al. (2020) further validate this statement using the vector Kirchhoff integral equation. A major difference in particle geometry between smooth and roughened ice crystals is the sizes of the individual planar facets of a particle. With L defined as the maximum length of a facet of an ice crystal, we obtain $L^2\lambda \gg kD$ for a smooth ice crystal with $L = 23.19$ μm but $L^2\lambda < kD$ for roughened ice crystals with $L = 0.58$ μm in the present case. From the geometric optics perspective, distinct halo peaks quantified with IITM imply that the refraction of electromagnetic waves is determined mainly by the macroscopic shape rather than the small facets of the ice crystal rough surface, when the surface roughness is not significant and has a scale comparable to λ. For better understanding of these halo peaks for a roughened ice crystal from the physical perspective, the Debye series expansion of the T-matrix (Bi et al., 2018; Bi & Gouesbet, 2022) may be a useful approach.

3.2 Lidar backscattering properties

The lidar ratio S and depolarization ratio δ are two fundamental backscattering properties for lidar-based remote sensing applications. For a single ice crystal, these ratios are defined as

$$S = \frac{4\pi}{\omega P_{11}(\pi)}, \tag{2}$$

$$\delta = \frac{P_{11}(\pi) - P_{22}(\pi)}{P_{11}(\pi) + P_{22}(\pi)}. \quad (3)$$

Figures 3a–b plot the lidar and depolarization ratios associated with roughened ice crystals computed with IITM and IGOM+CBE and the counterparts associated with smooth ice crystals computed with IITM and PGOM. In Fig. 3a, the lidar ratios of roughened ice crystals substantially deviate from those of smooth ice crystals with size parameters $kD > 100$. In the range of kD up to 316 simulated with IITM (corresponding to D up to 26.8 μm at wavelength 532 nm), a decreasing lidar ratio with larger size parameters for smooth ice crystals originates presumably from the significant contribution of the second-order corner reflection (Borovoi et al., 2013). In Fig. 3b, the depolarization ratios exhibit pronounced sensitivities to the degree of surface roughness for size parameters $kD > 20$. The depolarization ratio levels off between 0.2 for smooth and 0.55 for severely roughened ice crystals with $kD \geq 100$.

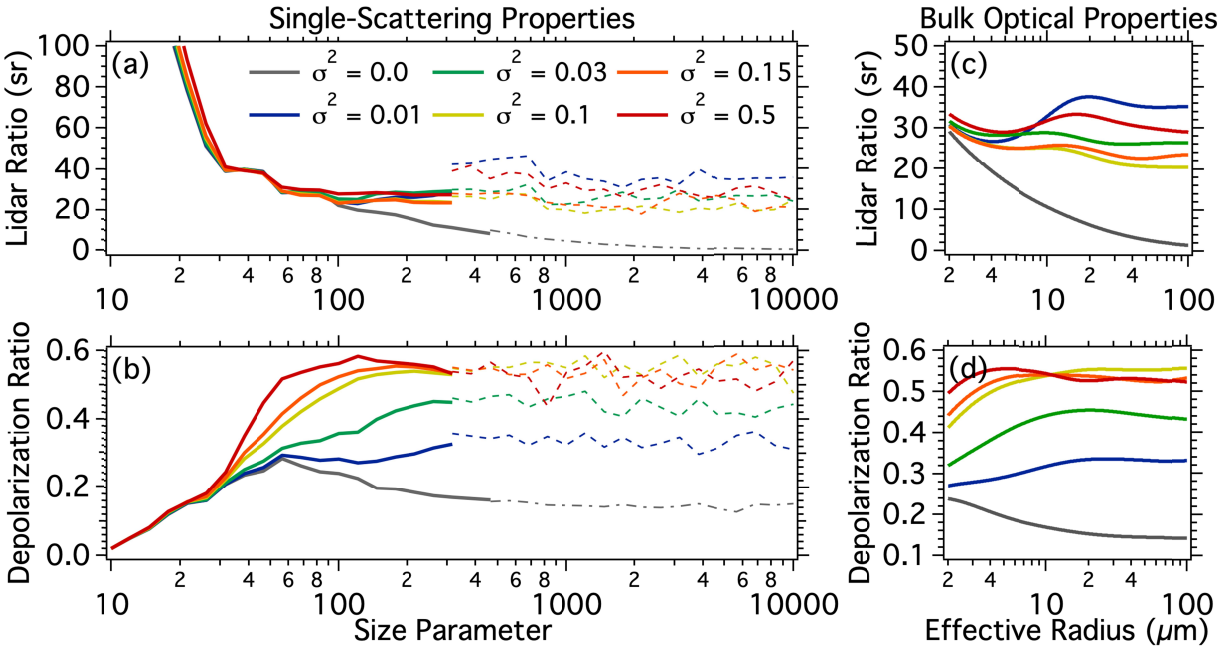

Figure 3. The single-scattering (a) lidar and (b) depolarization ratios (y-axis scales), for various degrees of surface roughness (colors stated in (a)) computed with (bold solid lines) rigorous and

184 (dashed lines) geometric optics methods, for size parameters 10 to 10000 (x-axis scales). (c-d)
185 Bulk optical properties corresponding to (a-b), for effective radius 2 to 100 μm (x-axis scales).

186

187 The backscattering properties of roughened ice crystals computed with IGOM+CBE are
188 consistent with IITM at the size parameter upper limit, except with lidar ratios (Fig. 3a) for
189 $\sigma^2 = 0.01$ and 0.5 that may be associated with simplified assumptions in the CBE correction.
190 Because of weak ice absorptivity at wavelength 532 nm, the backscattering properties tend to
191 approach their respective asymptotic values for larger size parameters, as indicated by
192 IGOM+CBE simulations. In Fig. 3b, moderate fluctuations in the IGOM+CBE backscattering
193 properties originate from Monte Carlo noise associated with the ray-tracing process (Saito &
194 Yang, 2022b).

195 Bulk optical properties of polydisperse ice crystals are obtained from a weighted average
196 over the single-scattering properties of smooth and roughened ice crystals. The particle size
197 distribution (PSD) is assumed to be a gamma distribution with an effective variance of 0.26
198 (Saito & Yang, 2022a) obtained from in-situ observations of ice cloud PSDs (Heymsfield et al.,
199 2013). The bulk lidar and depolarization ratios of the polydisperse ice crystals are computed
200 based on Eqs. (1–2) with replacing the single-scattering properties with the bulk ice crystal
201 counterparts. Figures 3c–d show the bulk backscattering properties of smooth and roughened
202 hexagonal column ice crystals for effective radii 2–100 μm. The backscattering properties of
203 roughened ice crystals show a weak dependence on effective radius > 20 μm. In contrast, those
204 of a smooth ice crystal consistently show a negative correlation with effective radius.

205

3.3 Comparison with spaceborne lidar observations

We compare the theoretical backscattering properties of smooth and roughened ice crystals with the counterparts estimated from the Cloud-Aerosol Lidar with Orthogonal Polarization (CALIOP) observations (Winker et al., 2009). We use the version 4.20 CALIOP level-2 cloud layer 5km product and select single-layer transparent cirrus clouds with a middle cloud temperature $T \leq -60$ °C, where ice particles are typically small (Platt et al., 1987, 2002) as less water vapor is available for ice crystal growth in a colder atmosphere. The lidar ratio is derived from the constrained retrievals utilizing the two-way transmissivity of ice clouds (Young & Vaughan, 2009). The particulate depolarization ratio is derived from the measured volume depolarization ratio with the Rayleigh scattering contribution subtracted (Hu et al., 2009).

Figure 4 shows the climatological distributions of the lidar and depolarization ratios of cold cirrus clouds observed by CALIOP in 2009. CALIOP points in an off-nadir direction to avoid substantial influence from horizontally aligned ice crystals (Saito & Yang, 2019) in the present analysis. The observed lidar and depolarization ratios are densely populated in a range S of 10–45 sr and δ of 0.3–0.6. The backscattering properties of smooth ice crystals are far from this range, but those of roughened ice crystals ($\sigma^2 = 0.01$–0.5, and especially 0.03–0.15) tend to be within the range. Interestingly, this roughness range is also consistent with a range of estimated surface roughness from 0.01–0.3 using stereographic SEM measurements of ice crystals in a laboratory (Neshyba et al., 2013, Butterfield et al., 2017).

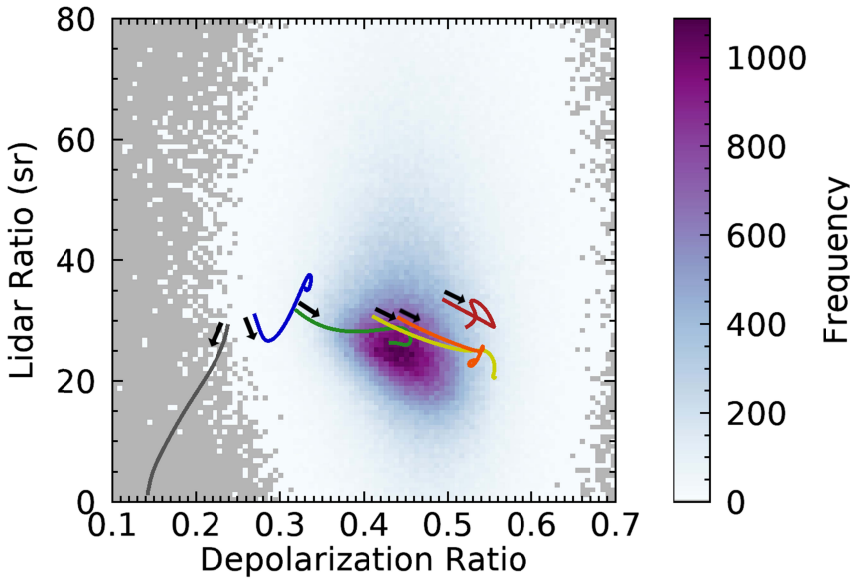

225

226 **Figure 4**. Two-dimensional histogram of the lidar and depolarization ratios of cold cirrus clouds
227 obtained from CALIOP observations in 2009. Color lines are the theoretical counterparts along
228 effective radii from 2–100 μm (arrows show the 2-μm starting points) with various degrees of
229 surface roughness (same colors as in Figs. 2 and 3).

230

231 Previous studies show that smooth ice crystals with various aspect ratios exhibit limited
232 variations of δ from 0.1–0.2 (Borovoi et al. 2013), with the exception of a smooth droxtal that
233 shows lidar and depolarization ratios ranging from 30–40 sr and approximately 0.4, respectively
234 (Okamoto et al., 2020). However, smooth droxtals are considered to be rare in ice clouds, as they
235 produce specific halo peaks (Zhang et al., 2004) that are rarely observed (Sassen et al., 2003).
236 This suggests that droxtals in ice clouds have some degree of surface roughness. Thus, we
237 conclude that surface roughness has pronounced impacts on the backscattering properties of ice
238 crystals and must be considered to infer the microphysical properties of ice clouds from lidar
239 backscattering signals.

Reichardt et al. (2002) reported two distinct correlations among the lidar ratio, depolarization ratio, and temperature of cirrus clouds from ground-based lidar observations. A strong positive correlation between the lidar and depolarization ratios occurring at warmer temperatures (above -40°C) is well explained by the presence of horizontally oriented planar ice crystals (e.g., Saito et al., 2017). However, a reported slight negative correlation between the lidar and depolarization ratios occurring at colder temperatures (below -50°C) has been an open question. Figure 5 shows correlations among backscattering properties, temperature, and surface roughness obtained from CALIOP observations of single-layer transparent cirrus clouds with $T \leq -40$ °C and theoretical backscattering simulations. The roughness variations can mimic the temperature dependence of the CALIOP-based backscattering properties of ice clouds. Although a definitive conclusion cannot be obtained from this analysis, a potential temperature dependence of the surface roughness of ice crystals could be a candidate to explain the slight anti-correlation of the lidar and depolarization ratios of cold cirrus clouds.

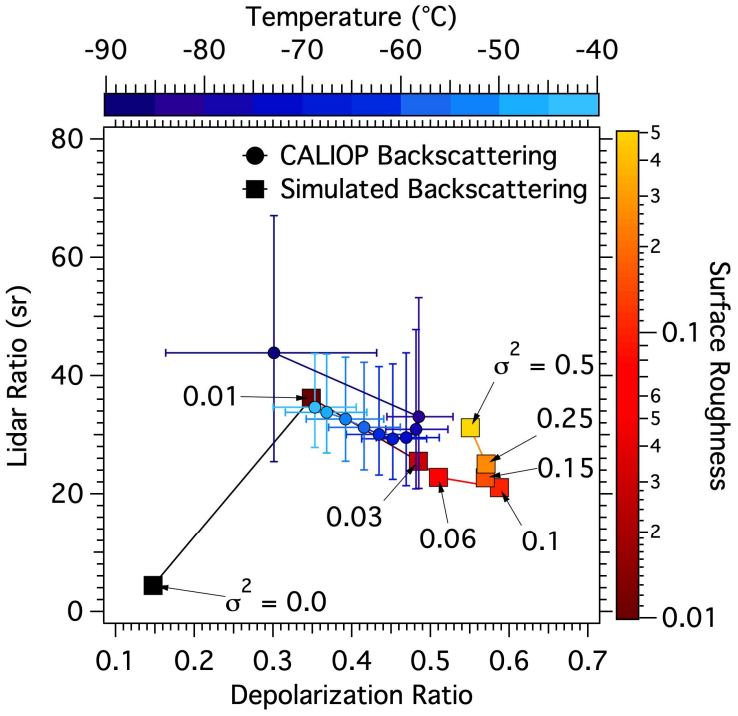

Figure 5. (circles) Median and quartile ranges of the lidar and depolarization ratios of ice clouds with various middle cloud temperatures (indicated by blue colors) obtained from CALIOP observations. (squares) Theoretical counterparts with various degrees of surface roughness (indicated by red colors) and an effective radius of 30 μm are coplotted.

4 Conclusions

This study performs single-scattering property simulations of smooth and roughened hexagonal column ice crystals over a wide size parameter range to investigate the impact of surface roughness on backscattering properties. State-of-the-science light-scattering computational methods and realistic ice crystal models reveal distinct differences in the lidar ratio between smooth and roughened ice crystals. The depolarization ratio is especially sensitive to the degree of surface roughness. Comparisons between theoretical backscattering properties with various degrees of surface roughness and those estimated from CALIOP observations imply that surface roughness is essential to robust explanation of observed lidar backscattering signals associated with cold cirrus clouds, and imply possible temperature dependence of dominant degrees of surface roughness of ice crystals.

The present study indicates a robust path forward for a better interpretation of lidar-derived backscattering signals by using the microphysical properties of ice crystals. Further research using sophisticated polarimetric lidar observations and these ice crystal backscattering property models should provide knowledge of a wider range of morphological characteristics of ice clouds.

Acknowledgments

This research was supported by NASA Grant NNH18ZD001N-RST and partly by endowment funds related to the David Bullock Harris Chair in Geosciences at the College of Geosciences, Texas A&M University (grant number 02-512231-0001). The numerical computations were conducted with high-performance computing resources provided by Texas A&M University (https://hprc.tamu.edu).

Open Research

The single and bulk scattering property data used in this study will be publicly available (https://doi.org/10.5281/zenodo.??????) after the acceptance of this manuscript (the data is temporarily available from Supplemental Information). CALIOP data are available through the NASA Langley Research Center Atmospheric Science Data Center (https://asdc.larc.nasa.gov/).

References

Bi, L., & Gouesbet, G. (2022). Debye-series expansion of T-matrix for light scattering by nonspherical particles computed from Riccati-differential equations. *Optics Express*, 30, 29796–29810, doi:10.1364/OE.465772.

Bi, L., & Yang, P. (2014). Accurate simulation of the optical properties of atmospheric ice crystals with the invariant imbedding T-matrix method. *Journal of Quantitative Spectroscopy and Radiative Transfer,* 138, 17–35, doi:10.1016/j.jqsrt.2014.01.013.

296 Bi, L., Xu, F., & Gouesbet, G. (2018). Depolarization of nearly spherical particles: The Debye
297 series approach. *Physical Review A,* 98(5), 053809.
298 Borovoi, A., Konoshonkin, A., and Kustova, N. (2013). Backscattering by hexagonal ice crystals
299 of cirrus clouds, *Optics Letters,* 38, 2881–2884.
300 Butterfield, N., Rowe, P. M., Stewart, E., Roesel, D., & Neshyba, S. (2017). Quantitative three-
301 dimensional ice roughness from scanning electron microscopy. *Journal of Geophysical*
302 *Research: Atmospheres,* 122, 3023–3041.
303 Cox, C., & Munk, W. (1954). Measurement of the roughness of the sea surface from
304 photographs of the sun's glitter. *Journal of the Optical Society of America* 44(11), 838-
305 850.
306 Cross, J. D. (1968). Study of the surface of ice with a scanning electron microscope, In *Physics*
307 *of Ice*. Munich: Plenum Press, 81–94.
308 Ding, J., Yang, P., Holz, R. E., Platnick, S., Meyer, K. G., Vaughan, M. A., et al. (2016). Ice
309 cloud backscatter study and comparison with CALIPSO and MODIS satellite data, *Optics*
310 *Express*, 24, 620–636, https://doi.org/10.1364/OE.24.000620.
311 Ding, J., Yang, P., Mishchenko, M. I., & Nevels, R. D. (2020). Identify the limits of geometric
312 optics ray tracing by numerically solving the vector Kirchhoff integral, *Optics*
313 *Express*, 28, 10670–10682, doi:10.1364/OE.389097.
314 Heymsfield, A. J., Schmitt, C., & Bansemer, A. (2013). Ice cloud particle size distributions and
315 pressure-dependent terminal velocities from in situ observations at temperatures from 0
316 to −86°C. *Journal of the Atmospheric Sciences,* 70(12), 4123-4154.
317 Hioki, S., Yang, P., Baum, B. A., Platnick, S., Meyer, K. G., King, M. D., & Riedi, J. (2016).
318 Degree of ice particle surface roughness inferred from polarimetric observations,

Atmospheric Chemistry and Physics, 16, 7545–7558, https://doi.org/10.5194/acp-16-7545-2016.

Hu, Y., Winker, D., Vaughan, M., Lin, B., Omar, A., Trepte, C., et al. (2009). CALIPSO/CALIOP cloud phase discrimination algorithm, *Journal of Atmospheric and Oceanic Technology,* 26, 2293–2309, https://doi.org/10.1175/2009JTECHA1280.1.

Järvinen, E., Jourdan, O., Neubauer, D., Yao, B., Liu, C., Andreae, M. O., et al. (2018). Additional global climate cooling by clouds due to ice crystal complexity, *Atmospheric Chemistry and Physics*, 18, 15767–15781, https://doi.org/10.5194/acp-18-15767- 2018.

Johnson B. R. (1988). Invariant imbedding T-matrix approach to electromagnetic scattering. *Applied Optics*, 27, 4861–4873.

Liu, C., Panetta, R. L., & Yang, P. (2013). The effects of surface roughness on the scattering properties of hexagonal columns with sizes from the Rayleigh to the geometric optics regimes, *Journal of Quantitative Spectroscopy and Radiative Transfer,* 129, 169–185, https://doi.org/10.1016/j.jqsrt.2013.06.011.

Macke, A., Mueller, J., & Raschke, E. (1996). Single scattering properties of atmospheric ice crystals. *Journal of the Atmospheric Sciences,* 53(19), 2813–2825.

Magee, N., Boaggio, K., Staskiewicz, S., Lynn, A., Zhao, X., Tusay, N., et al. (2021). Captured cirrus ice particles in high definition, *Atmospheric Chemistry and Physics*, 21, 7171–7185, https://doi.org/10.5194/acp-21-7171-2021.

Magee, N. B., Miller, A., Amaral, M., & Cumiskey, A. (2014). Mesoscopic surface roughness of ice crystals pervasive across a wide range of ice crystal conditions, *Atmospheric Chemistry and Physics*, 14, 12357– 12371, doi:10.5194/acp-14-12357-2014.

Neshyba, S., Lowen, B., Benning, M., Lawson, A., & Rowe, P. (2013). Roughness metrics of prismatic facets of ice, *Journal of Geophysical Research: Atmospheres,* 118, 3309–3318.

Okamoto, H., Sato, K., Borovoi, A., Ishimoto, H., Masuda, K., Konoshonkin, A., & Kustova, N. (2020). Wavelength dependence of ice cloud backscatter properties for spaceborne polarization lidar applications. *Optics Express*, 28(20), 29178–29191. https://doi.org/10.1364/ OE.400510.

Pfalzgraff, W. C., Hulscher, R. M., & Neshyba, S. P. (2010). Scanning electron microscopy and molecular dynamics of surfaces of growing and ablating hexagonal ice crystals, *Atmospheric Chemistry and Physics*, 10, 2927–2935, doi:10.5194/acp-10-2927-2010.

Platt, C. M. R., Scott, S., & Dilley, A. (1987). Remote sounding of high clouds: IV. Optical properties of midlatitude and tropical cirrus, *Journal of the Atmospheric Sciences,* 44, 729–747.

Platt, C. M. R., Young, S. A., Austin, R. T., Patterson, G. R., Mitchell, D. L., & Miller, S. D. (2002). LIRAD observations of tropical cirrus clouds in MCTEX. Part I: Optical properties and detection of small particles in cold cirrus, *Journal of the Atmospheric Sciences,* 59, 3145–3162.

Reichardt, J., Reichardt, S., Behrendt, A., & McGee, T. (2002). Correlations among the optical properties of cirrus-cloud particles: Implications for spaceborne remote sensing, *Geophysical Research Letters*, 29, 140000–140001.

Saito M, & Yang P. (2019). Oriented ice crystals: a single-scattering property database for applications to lidar and optical phenomenon simulations. *Journal of the Atmospheric Sciences,* 76, 2635–2652.

363 Saito M, & Yang, P. (2022a). Generalization of atmospheric nonspherical particle size:
364 Interconversions of size distributions and optical equivalence, *Journal of the Atmospheric*
365 *Sciences,* 79, 3333–3349.
366 Saito, M., & Yang, P. (2022b). Critical Impacts of the Small-Scale Surface Roughness of Ice
367 Crystals on Lidar Backscattering Signals. 16th Conference on Atmospheric Radiation,
368 Madison, WI, American Meteorological Society, Session 8.2,
369 https://ams.confex.com/ams/CMM2022/meetingapp.cgi/Paper/404577.
370 Saito, M., Iwabuchi, H., Yang, P., Tang, G., King, M. D., & Sekiguchi, M. (2017). Ice particle
371 morphology and microphysical properties of cirrus clouds inferred from combined
372 CALIOP-IIR measurement, *Journal of Geophysical Research: Atmospheres,* 122, 4440–
373 4462, https://doi.org/10.1002/2016JD026080.
374 Sassen, K., Zhu, J., & Benson, S. (2003). Midlatitude cirrus cloud climatology from the Facility
375 for Atmospheric Remote Sensing, IV. Optical displays, *Applied Optics*, 42, 332–341,
376 https://doi.org/10.1364/AO.42.000332.
377 Schnaiter, M., Järvinen, E., Vochezer, P., Abdelmonem, A., Wagner, R., Jourdan, O., et al.
378 (2016). Cloud chamber experiments on the origin of ice crystal complexity in cirrus
379 clouds, *Atmospheric Chemistry and Physics*, 16, 5091–5110, https://doi.org/10.5194/acp-
380 16-5091-2016.
381 Ulanowski, Z., Kaye, P. H., Hirst, E., Greenaway, R. S., Cotton, R. J., Hesse, E., & Collier, C. T.
382 (2014). Incidence of rough and irregular atmospheric ice particles from Small Ice
383 Detector 3 measurements, *Atmospheric Chemistry and Physics*, 14, 1649–1662,
384 https://doi.org/10.5194/acp-14-1649-2014.
385 van de Hulst, H. C.: *Light Scattering by Small Particles.* John Wiley and Sons, 470 pp, 1957.

van Diedenhoven, B. (2014). The prevalence of the 22° halo in cirrus clouds, *Journal of Quantitative Spectroscopy and Radiative Transfer,* 146, 475–479.

van Diedenhoven, B., Ackerman, A. S., Fridlind, A. M., Cairns, B., & Riedi, J. (2020). Global statistics of ice microphysical and optical properties at tops of optically thick ice clouds. *Journal of Geophysical Research: Atmospheres,* 125, e2019JD031811. https://doi.org/10.1029/2019JD031811.

van Diedenhoven, B., Cairns, B., Fridlind, A. M., Ackerman, A. S., & Garrett, T. J. (2013). Remote sensing of ice crystal asymmetry parameter using multi-directional polarization measurements – Part 2: Application to the Research Scanning Polarimeter, *Atmospheric Chemistry and Physics*, 13, 3185–3203, https://doi.org/10.5194/acp- 13-3185-2013.

Winker, D. M., Vaughan, M. A. Omar, A. Hu, Y. Powell, K. A. Liu, Z. et al. (2009). Overview of the CALIPSO mission and CALIOP data processing algorithms, *Journal of Atmospheric and Oceanic Technology,* 26, 2310–2323.

Yang, P., & Liou, K. N. (1996). Geometric-optics-integral-equation method for light scattering by nonspherical ice crystals, *Applied Optics*, 35, 6568–6584.

Yang, P., & Liou, K. N. (1997). Light scattering by hexagonal ice crystals: Solution by a ray-by-ray integration algorithm, *Journal of the Optical Society of America A.*, 14, 2278-2289.

Yang, P. & Liou, K. N. (1998). Single-scattering properties of complex ice crystals in terrestrial atmosphere, *Contributions to Atmospheric Physics,* 71 (2), 223–248.

Yang, P., Ding, J., Panetta, R. L., Liou, K.-N., Kattawar, G. W., & Mishchenko, M. I. (2019). On the convergence of numerical computations for both exact and approximate solutions for electromagnetic scattering by nonspherical dielectric particles, *Progress in Electromagnetic Research*, 164, 27–61.

409 Yang, P., Hong, G., Kattawar, G. W., Minnis, P., & Yongxiang, H. (2008). Uncertainties
410 associated with the surface texture of ice particles in satellite-based retrieval of cirrus
411 clouds: Part II; Effect of particle surface roughness on retrieved cloud optical thickness
412 and effective particle size, *IEEE Transactions on Geosciences and Remote Sensing* 46,
413 1948–1957.
414 Yi, B., Yang, P., Baum, B. A., L'Ecuyer, T., Oreopoulos, L., Mlawer, E. Jet al. (2013). Influence
415 of ice particle surface roughening on the global cloud radiative effect, *Journal of the*
416 *Atmospheric Sciences,* 70, 2794–2807.
417 Young, S. A. & Vaughan, M. A. (2009). The retrieval of profiles of particulate extinction from
418 Cloud Aerosol Lidar Infrared Pathfinder Satellite Observations (CALIPSO) data:
419 Algorithm description, *Journal of Atmospheric and Oceanic Technology,* 26, 1105–1119,
420 https://doi.org/10.1175/2008JTECHA1221.1.
421 Zhang, Z., Yang, P., Kattawar, G. W., Tsay, S.-C., Baum, B. A., Huang, et al. (2004), Geometric
422 optics solution to light scattering by droxtal ice crystals, *Applied Optics*, 43, 2490–2499,
423 doi:10.1364/AO.43.002490.
424 Zhou, C. & Yang, P. (2015). Backscattering peak of ice cloud particles, *Optics Express*, 23,
425 11995–12003.